AIAA Regional Student Conferences
, Multiple Locations
2025 Regional Student Conferences

10.2514/6.2025-97508

The Spectral Difference with Divergence Cleaning Method for 3D Simulations of Solar Magnetic Cycles

Russell J. Hankey* and Chunlei Liang †
Clarkson University, Potsdam, New York, USA

The spectral difference method is a versatile high-order method that has shown its high-order accuracy and robustness to predict compressible viscous flows on structured multidomain and unstructured grids [1–3]. The spectral difference method can also be massively parallelized to solve nonlinear MHD problems [4, 5]. In this study, the Spectral Difference with Divergence Cleaning (SDDC) method is further developed to solve several three-dimensional kinematic dynamo problems. The first kinematic dynamo problem is solved in a cubic periodic box, where the SDDC method is successfully verified to capture the 'Cigar' structures published in the literature [6]. The second kinematic dynamo problem adopts a spherical shell geometry [7] and perfectly conducting and perfectly radial boundary conditions [8, 9] to solve three-dimensional induction equations. Finally, the SDDC method is employed to model Sunspot cycles.

I. Introduction

Fully three-dimensional magnetohydrodynamics (MHD) models of the solar dynamo are computationally expensive and can not yet capture the full complexity of flux emergence and the Babcock–Leighton (BL) mechanism. To capture the effects of emerging flux tubes and the evolution of the resulting bipolar magnetic regions (BMRs), Yeates and Muñoz [9] adopted a kinematic framework in which the flow field is specified and only the induction equation is simulated. In their work, Yeates and Muñoz designed a "lift and twist" algorithm for modeling the emerging flux tubes. Miesch and his collaborators [8, 10, 11] developed a 3D Babcock-Leighton / flux transport dynamo model in which the source of the poloidal field is the explicit emergence, distortion, and dispersal of bipolar magnetic regions (BMR) that was supported by a "SpotMaker" algorithm. Since Yeates and Muñoz's work, different prescribed flow fields have been explored in an attempt to match the evolution of observed BMRs [11].

Yeates and Muñoz's work uses finite differences in a spherical shell to solve the magnetic potential equation, which requires a structured grid, is difficult to parallelize, and requires additional work to extend to higher orders. Miesch's STABLE code [8] is again structured but is based on the Spherical Harmonics method, which has high-order accuracy. Application of the spectral difference method to this problem would allow the use of unstructured grids, easy parallelization for high-performance computers with heterogeneous architectures, and simple extension to higher orders. The spectral difference divergence cleaning algorithm (SDDC) was proposed and applied to the magnetic induction equation in Chen and Liang [4] using a divergence cleaning technique to keep $\nabla \cdot \mathbf{B}$ close to zero. The Spectral Difference method was also integrated with a transfinite mapping algorithm and cubed-sphere grids in Chen et al. [7] to predict interior convection for some solar benchmark problems. To the best knowledge of the authors, our research is the first time SDDC has been applied to 3D induction equations. In this paper, a three-dimensional Spectral Difference Solar Dynamo (SD^2) code is developed by integrating the spectral difference method with the same cubed-sphere mesh generator and transfinite mapping for massively parallel solutions of kinematic dynamo equations on GPUs.

This paper is organized as follows. Section II presents the equations that are used to simulate the kinematic dynamo for this work. Section III introduces the spectral difference method. Section IV presents the solar dynamo problem studied in this work.

---

*AIAA Student Member, Department of Mechanical and Aerospace Engineering, Clarkson University, hankeyrj@clarkson.edu, AIAA Member Number: 1192687, AIAA Member Type: Regular Graduate Student

†AIAA Associate Fellow, Professor of Mechanical and Aerospace Engineering, Clarkson University, cliang@clarkson.edu, AIAA Member Number: 303971

II. Governing Equations

A. The Induction Equation

The magnetic induction equation used in kinematic dynamo models is written as

$$\frac{\partial \mathbf{B}}{\partial t} = \nabla \times (\mathbf{U} \times \mathbf{B}) - \nabla \times (\eta_t \nabla \times \mathbf{B}), \tag{1}$$

where $\mathbf{B} = (Bx, By, Bz)^{\mathbf{T}}$ is the magnetic field, $\mathbf{U} = (u, v, w)^{\mathbf{T}}$ is the velocity profile, and η is the magnetic resistivity. The spectral difference method requires the governing equations to be written in divergence form

$$\frac{\partial \mathbf{Q}}{\partial t} + \nabla \cdot \mathbf{F} = \mathbf{M}, \tag{2}$$

where $\mathbf{Q} = \mathbf{B}$ is the vector of conserved variables and $\mathbf{M} = \mathbf{0}$ is vector of non-conservative terms. The total flux $\mathbf{F} = \mathbf{F}_{inv} - \mathbf{F}_{vis}$ consists of the inviscid fluxes minus the viscous fluxes. The inviscid flux vector ($\mathbf{F}_{inv}$) and viscous flux vector ($\mathbf{F}_{vis}$) are

$$\mathbf{F}_{inv}(\mathbf{Q}) = \mathbf{U} \otimes \mathbf{B} - \mathbf{B} \otimes \mathbf{U}, \quad \mathbf{F}_{vis}(\nabla \mathbf{Q}) = \eta_t \left((\nabla \mathbf{B})^{\mathbf{T}} - \nabla \mathbf{B} \right). \tag{3}$$

B. Divergence Cleaning

The following generalized Lagrange multiplier (GLM) approach used is introduced in [12] and implemented by Chen & Liang (2022) in [4] for the resistive MHD equations, although we are only using the induction equation

$$\frac{\partial}{\partial t} \begin{bmatrix} \mathbf{B} \\ \psi \end{bmatrix} + \nabla \cdot \begin{bmatrix} \mathbf{U} \otimes \mathbf{B} - \mathbf{B} \otimes \mathbf{U} - \eta_t \left((\nabla \mathbf{B})^{\mathbf{T}} - \nabla \mathbf{B} \right) + c_h \psi \mathtt{I} \\ c_h \mathbf{B} \end{bmatrix} = - \begin{bmatrix} (\nabla \cdot \mathbf{B}) \mathbf{U} \\ (\nabla \psi) \cdot \mathbf{U} + \alpha \psi \end{bmatrix}, \tag{4}$$

where $\mathtt{I}$ is the identity matrix. In these equations, $\mathbf{Q} = (\mathbf{B},\ \psi)^{\mathbf{T}}$, $\mathbf{M} = ((\nabla \cdot \mathbf{B})\mathbf{U},\ (\nabla \psi) \cdot \mathbf{U} + \alpha \psi)^{\mathbf{T}}$, $\mathbf{F}_{inv}(\mathbf{Q}) = (\mathbf{U} \otimes \mathbf{B} - \mathbf{B} \otimes \mathbf{U} + c_h \psi \mathtt{I},\ c_h \mathbf{B})^{\mathbf{T}}$, and $\mathbf{F}_{vis}(\nabla \mathbf{Q}) = (\eta_t \left((\nabla \mathbf{B})^{\mathbf{T}} - \nabla \mathbf{B} \right),\ 0)^{\mathbf{T}}$.

The new scalar ψ couples the divergence-free condition with the induction equation. The hyperbolic divergence cleaning speed c_h is chosen to be a multiple of the maximum velocity $c_h = w_{spd} \max_{\Omega} (\sqrt{u^2 + v^2 + w^2})$, where w_{spd} is a problem-specific constant. The first non-conservative source term is the induction portion of the Powell source vector [13] that arises naturally in the derivation of the induction equation if $\nabla \cdot \mathbf{B}$ is not assumed to be zero, and the second non-conservative term, $-\alpha \psi$, ensures that ψ decays in the region where $\nabla \cdot \mathbf{B} \approx 0$. α is another problem-specific constant defined as the parabolic diffusion rate which controls the damping of the field ψ.

III. Numerical Methods

A. The Spectral Difference Method

We use the spectral difference method to solve the equations spatially. Each hexahedral element is mapped from the physical domain to the standard cube element in the computational domain ($0 \leq \xi \leq 1, 0 \leq \eta \leq 1, 0 \leq \zeta \leq 1$). A two-dimensional representation of this mapping is shown in Fig. 1a where quadrilateral elements are shown instead of hexahedral elements for simplicity. The transformation is represented by

$$\begin{pmatrix} x \\ y \\ z \end{pmatrix} = \sum_{i=1}^{K} M_i(\xi, \eta, \zeta) \begin{pmatrix} x_i \\ y_i \\ z_i \end{pmatrix}, \tag{5}$$

where K is the number of nodes used to define an element, (x_i, y_i, z_i) are the nodal coordinates, and $M_i(\xi, \eta, \zeta)$ is the shape function for node i. We use the transfinite mapping explored in section 4A of [7] to reduce the error generated by the mapping. After the transformation, the conservation law takes the form

$$\frac{\partial \tilde{\mathbf{Q}}}{\partial t} + \frac{\partial \tilde{\mathbf{F}}}{\partial \xi} + \frac{\partial \tilde{\mathbf{G}}}{\partial \eta} + \frac{\partial \tilde{\mathbf{H}}}{\partial \zeta} + \tilde{\mathbf{M}} = 0, \tag{6}$$

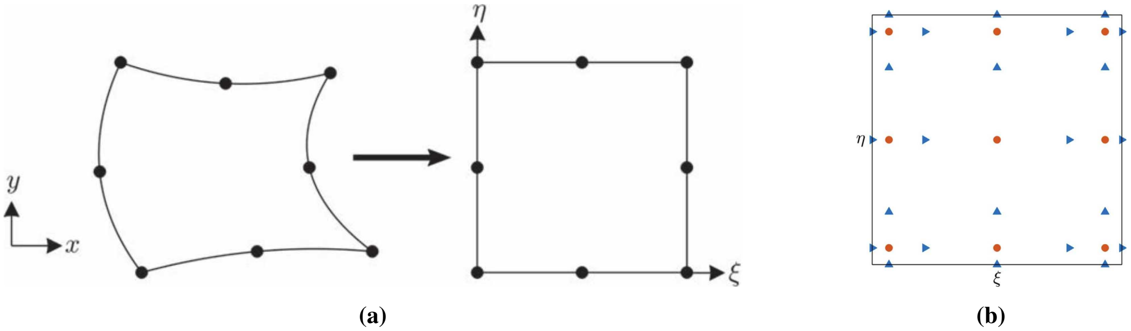

(a) (b)

Fig. 1 Panel (a) shows the transformation between physical and computational domains for a quadrilateral element. Panel (b) shows the solution points (circles) and flux points (triangles) for $N = 3$ in an element, where right-pointing triangles are FPs in the ξ direction and upward-pointing triangles are FPs in the η direction.

with $\tilde{\mathbf{Q}} = |J|\mathbf{Q}$, $\tilde{\mathbf{M}} = |J|\mathbf{M}$, and

$$\begin{pmatrix}\tilde{\mathbf{F}}\\ \tilde{\mathbf{G}}\\ \tilde{\mathbf{H}}\end{pmatrix} = |J|J^{-1}\begin{pmatrix}\mathbf{F}\\ \mathbf{G}\\ \mathbf{H}\end{pmatrix}, \quad \text{where } J = \frac{\partial(x,y,z)}{\partial(\xi,\eta,\zeta)} = \begin{bmatrix} x_\xi & x_\eta & x_\zeta \\ y_\xi & y_\eta & y_\zeta \\ z_\xi & z_\eta & z_\zeta \end{bmatrix}. \tag{7}$$

Solution points (SPs) and flux points (FPs) are defined in the standard computational element, where N SPs are used in each dimension to generate a polynomial of $(N-1)$ order in that dimension. A two-dimensional representation of this is shown for $N = 3$ SPs in Fig. 1b. The positions of the SPs (X_s) are the Chebyshev-Gauss points, which are defined as

$$X_s = \frac{1}{2}\left[1 - \cos\left(\frac{2s-1}{2N}\pi\right)\right], \quad s = 1, 2, \ldots, N. \tag{8}$$

The positions of the FPs (X_f) are chosen to be the $(N-1)$ roots of the Nth order Legendre polynomial plus the two boundaries, resulting in $(N+1)$ total FPs. In the computational domain our boundaries are $X_{f=1} = 0$ and $X_{f=N+1} = 1$, and an Nth order Legendre polynomial can be generated by

$$P_n(\xi) = \frac{2n-1}{n}(2\xi - 1)P_{n-1}(\xi) - \frac{n-1}{n}P_{n-2}(\xi) \tag{9}$$

where $P_{-1}(\xi) = 0$ and $P_0(\xi) = 1$ are the starting polynomials.

Polynomials representing the conserved quantities are constructed over the SPs and FPs through the application of Lagrange bases

$$h_i(X) = \prod_{s=1,\ s\neq i}^{N}\left(\frac{X - X_s}{X_i - X_s}\right), \quad l_i(X) = \prod_{f=1,\ f\neq i}^{N+1}\left(\frac{X - X_f}{X_i - X_f}\right). \tag{10}$$

The reconstructed solution to the conserved quantities is then found through the tensor products of the three one-dimensional Lagrange bases

$$\mathbf{Q} = \sum_{k=1}^{N}\sum_{j=1}^{N}\sum_{i=1}^{N}\frac{\tilde{\mathbf{Q}}_{i,j,k}}{|J_{i,j,k}|}h_i(\xi)\times h_j(\eta)\times h_k(\zeta). \tag{11}$$

The values of the conserved quantities at the FPs are used to calculate the fluxes at the FPs. The reconstructed flux polynomials are then found by

$$\tilde{\mathbf{F}} = \sum_{k=1}^{N}\sum_{j=1}^{N}\sum_{i=1}^{N+1} \tilde{\mathbf{F}}_{i,j,k} \times l_i(\xi) \times h_j(\eta) \times h_k(\zeta), \tag{12}$$

$$\tilde{\mathbf{G}} = \sum_{k=1}^{N}\sum_{j=1}^{N+1}\sum_{i=1}^{N} \tilde{\mathbf{G}}_{i,j,k} \times h_i(\xi) \times l_j(\eta) \times h_k(\zeta), \tag{13}$$

$$\tilde{\mathbf{H}} = \sum_{k=1}^{N+1}\sum_{j=1}^{N}\sum_{i=1}^{N} \tilde{\mathbf{H}}_{i,j,k} \times h_i(\xi) \times h_j(\eta) \times l_k(\zeta). \tag{14}$$

Reconstructing the solution and fluxes this way produces polynomials that are continuous in each element but discontinuous at element interfaces. We use the Rusanov solver [14] (also called the local Lax-Friedrichs solver [15]) to compute common inviscid fluxes at the element interfaces in the normal direction in the computational domain. To compute gradients of conserved variables, we need the interpolated conserved quantities to be continuous across element interfaces as well, which is accomplished through the application of the BR1 [16] scheme that takes the average between the left and right cells. The gradients of the conserved variables are then calculated following the method proposed by Sun et al. [2] using the FPs and are stored on the SPs, then extrapolated to the FPs for the computation of the viscous fluxes. The derivatives of the fluxes are then calculated using the derivative of the Lagrange basis l

$$\left.\frac{\partial \tilde{\mathbf{F}}}{\partial \xi}\right|_{i,j,k} = \sum_{r=1}^{N+1} \tilde{\mathbf{F}}_{r,j,k} \times l'_r(\xi_i), \tag{15}$$

$$\left.\frac{\partial \tilde{\mathbf{G}}}{\partial \eta}\right|_{i,j,k} = \sum_{r=1}^{N+1} \tilde{\mathbf{G}}_{i,r,k} \times l'_r(\eta_j). \tag{16}$$

$$\left.\frac{\partial \tilde{\mathbf{H}}}{\partial \zeta}\right|_{i,j,k} = \sum_{r=1}^{N+1} \tilde{\mathbf{H}}_{i,j,r} \times l'_r(\zeta_k). \tag{17}$$

B. Temporal Solver

After computing the spatial derivatives, the governing equations become ODEs in residual form

$$\left(\frac{d\tilde{\mathbf{Q}}}{dt}\right)_{i,j,k} = \mathbf{R}_{i,j,k}, \quad \mathbf{R}_{i,j,k} = -\left(\tilde{\mathbf{M}} + \frac{\partial \tilde{\mathbf{F}}}{\partial \xi} + \frac{\partial \tilde{\mathbf{G}}}{\partial \eta} + \frac{\partial \tilde{\mathbf{H}}}{\partial \zeta}\right)_{i,j,k}, \tag{18}$$

where $\mathbf{R}_{i,j,k}$ is the residual at a specific SP. The physical quantities of the conserved variables are related to the quantities in the computational domain by

$$\left(\frac{d\tilde{\mathbf{Q}}}{dt}\right)_{i,j,k} = |J_{i,j,k}| \left(\frac{d\mathbf{Q}}{dt}\right)_{i,j,k}. \tag{19}$$

Now, ODEs can be treated as standard initial value problems and solved with a generic time-stepping method. In this work, we use a four-stage 3rd-order Strong Stability Preserving Runge-Kutta (SSPRK) method whose coefficients are reported in [17].

IV. The Solar Dynamo Problem

The goal of this paper is to simulate the solar magnetic cycles using a kinematic dynamo model and the 3D spectral difference with divergence cleaning method to allow the use of unstructured grids, straightforward parallelization, and simple extension to higher orders. To simulate the solar dynamo problem, we need the following

- A spherical or oblate spherical shell mesh to model the solar convective zone.
- A high order mapping algorithm between the physical and computational spaces, where we choose transfinite mapping.
- A flow field for the solar convective zone.

- Method for producing bipolar magnetic regions (BMRs).
- Boundary conditions at the surface of the Sun and the base of the convective zone for the induction and GLM $\nabla \cdot \mathbf{B}$ correction equations.

We name the resulting code the Spectral Difference Solar Dynamo (SD^2) code.

A. Solar Dynamo Setup

The first things we need in order to start simulations on solar kinematic dynamos are a mesh for the convective region of the Sun and a way to map curved cells in physical space to computational space. Fortunately, both of these have been studied in [7] where a cubed sphere mesh is created for cells with more isotropic volumes than the more standard UV spheres, and the transfinite method is used to map the curved elements from physical space to computational space.

Next, we need to generate a flow field for the solar convective zone. We particularly appreciated section 3 in [18] for generating the meridional circulation profile correctly, and many other profiles have been studied [8–11, 18, 19]. We used the profile for differential rotation from Miesch and Tweldebirhan [8] and the profile for meridional circulation in Karak and Miesch [11].

The velocity field can be written as

$$\mathbf{U} = \mathbf{U}_{pol} + \mathbf{U}_{tor} = U_r(r,\theta)\hat{\mathbf{e}}_r + U_\theta(r,\theta)\hat{\mathbf{e}}_\theta + U_\phi(r,\theta)\hat{\mathbf{e}}_\phi \tag{20}$$

where $\mathbf{U}_{pol}$ is the poloidal velocity (also called meridional circulation), $\mathbf{U}_{tor}$ is the toroidal velocity (also called differential rotation), U_r is the radial component of velocity ($r = R_\odot = 695.7 \times 10^8$cm is the top boundary and $r = 0.69R_\odot$ is the bottom boundary), U_θ is the θ component of velocity (θ is the latitudinal coordinate where $\theta = 0$ is the north pole and $\theta = \pi$ is the south pole), and $U_\phi(r,\theta) = r\sin\theta\Omega(r,\theta)$ is the ϕ component of velocity (ϕ is the longitudinal coordinate). We convert spherical velocity to Cartesian velocity by

$$\begin{pmatrix} u \\ v \\ w \end{pmatrix} = \begin{pmatrix} \sin\theta\cos\phi & \cos\theta\cos\phi & -\sin\phi \\ \sin\theta\sin\phi & \cos\theta\sin\phi & \cos\phi \\ \cos\theta & -\sin\theta & 0 \end{pmatrix} \begin{pmatrix} U_r \\ U_\theta \\ U_\phi \end{pmatrix} \tag{21}$$

The differential rotation is given in [8] as

$$\Omega(r,\theta) = \Omega_c + \frac{1}{2}\left[1 + \mathrm{erf}\left(2\frac{r - r_c}{d}\right)\right](\Omega_s(\theta) - \Omega_c) \tag{22}$$

where $\Omega_c = 2\pi\nu_c$ is the differential rotation of the core and

$$\Omega_s(\theta) = 2\pi(\nu_{eq} + a_2\cos^2\theta + a_4\cos^4\theta) \tag{23}$$

where $\nu_c = 432.8$nHz, $\nu_{eq} = 460.7$nHz, $a_2 = -62.9$nHz, $a_4 = -67.13$nHz, $r_c = 0.7R_\odot$ and $d = 0.05R_\odot$. We use a rotating reference frame at the rotational speed of the core with the mesh to reduce the maximum flow velocity, so the differential rotation is implemented as

$$\Omega(r,\theta) = \frac{1}{2}\left[1 + \mathrm{erf}\left(2\frac{r - r_c}{d}\right)\right](\Omega_s(\theta) - \Omega_c). \tag{24}$$

The $U_\phi(r,\theta)$ that results is shown in Fig. 2c.

The meridional circulation is given in [20] for ψ_{flow} such that $\rho\mathbf{U}_{pol} = \nabla \times [\psi_{flow}(r,\theta)\hat{\mathbf{e}}_\phi]$, where $\rho = C\left(\frac{R_\odot}{r} - 0.95\right)^{3/2}$ and

$$\psi_{flow} r\sin\theta = \psi_{flow,0}(r - R_p)\sin\left[\frac{\pi(r - R_p)}{(R_\odot - R_p)}\right](1 - \exp[-\beta_1\theta^\epsilon])\left(1 - \exp\left[\beta_2\left(\theta - \frac{\pi}{2}\right)\right]\right)\exp\left[-\left(\frac{r - r_0}{\Gamma}\right)^2\right]. \tag{25}$$

The constants are $C = 1$, $\beta_1 = 1.5$, $\beta_2 = 1.3$, $\epsilon = 2.0000001$, $r_0 = 0.45R_\odot/3.5$, $\Gamma = 3.47 \times 10^{10}$cm, and $R_p = 0.69R_\odot$. The value of $\psi_{flow,0}/C = -1.9 \times 10^{13}$ so that the amplitude of meridional circulation at mid-latitudes becomes $18\frac{\mathrm{m}}{\mathrm{s}}$. We then follow [11] in applying a downward magnetic pumping term to the flow field defined as

$$\gamma_r(r) = -\frac{\gamma_{CZ}}{2}\left[1 + \mathrm{erf}\left(\frac{r - 0.725R_\odot}{0.01R_\odot}\right)\right] - \frac{\gamma_S}{2}\left[1 + \mathrm{erf}\left(\frac{r - 0.9R_\odot}{0.02R_\odot}\right)\right] \tag{26}$$

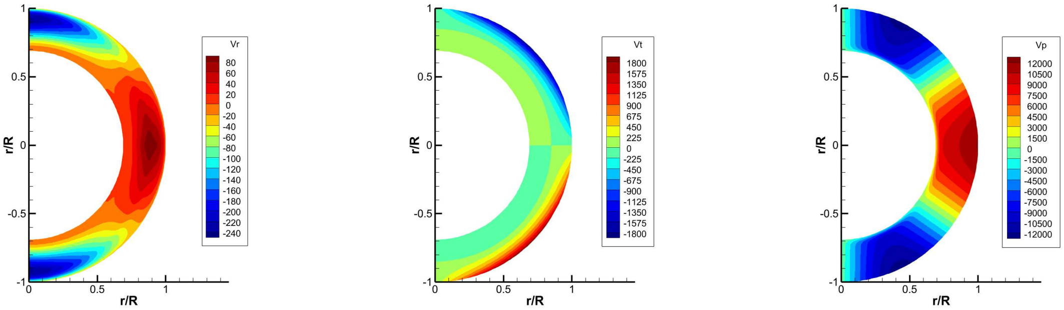

(a) Radial velocity component. **(b) Latitudinal velocity component.** **(c) Longitudinal velocity component.**

Fig. 2 Components of the velocity profile.

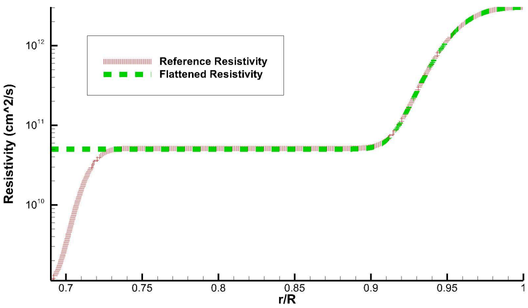

Fig. 3 Comparison between the resistivity profile we are using and the resistivity profile in [11].

such that Eqn. 20 becomes

$$\mathbf{U} = (U_r(r,\theta) + \gamma_r)\hat{\mathbf{e}}_r + U_\theta(r,\theta)\hat{\mathbf{e}}_\theta + U_\phi(r,\theta)\hat{\mathbf{e}}_\phi. \tag{27}$$

The resulting $U_r(r,\theta) + \gamma_r$ profile is shown in Fig. 2a and the $U_\theta(r,\theta)$ profile is shown in Fig. 2b.

Our resistivity profile is based on that provided in [11], but flattened within the cells touching the lower boundary, as shown in Fig. 3. This mitigates the necessity of many cells to resolve the resistivity gradient within the depth spanned by the first cell. The equation we use to produce our resistivity profile is

$$\eta_t(r) = \eta_{CZ} + \frac{\eta_S}{2}\left[1 + \operatorname{erf}\left(\frac{r - 0.956R_\odot}{0.025R_\odot}\right)\right] \tag{28}$$

where $\eta_{CZ} = 5 \times 10^{10}\,\frac{\text{cm}^2}{\text{s}}$ and $\eta_S = 3 \times 10^{12}\,\frac{\text{cm}^2}{\text{s}}$.

After the basic flow field has been defined, we need a way to produce BMRs. Yeates and Muoz [9] use a "lift and twist" perturbation of the flow to emulate the effects of magnetic buoyancy, while the STABLE code used in [8, 10, 11] places BMRs on the photosphere. For this paper, we implement the "lift and twist" flow from [9]. To implement the "lift and twist" flow, we need a center for the perturbation that gradually moves upward through the convective zone and velocity components that modify the existing flow field as if an emerging spot was present.

Working in spherical coordinates, we can say that the center of an emerging spot is given by $(\bar{r}, \bar{\theta}, \bar{\phi})$ and the distance between the center and an arbitrary point (r, θ, ϕ) is

$$\xi = \sqrt{r^2 + \bar{r}^2 - 2r\bar{r}(\sin\theta\sin\bar{\theta}\cos(\phi - \bar{\phi}) + \cos\theta\cos\bar{\theta})}. \tag{29}$$

The center is prescribed to move radially and longitudinally, but effects of meridional circulation are assumed to be negligible during the emergence of the spot. The equations for the velocity of the center of the spot are then

$$\frac{d\bar{r}}{dt} = u_0, \quad \frac{d\bar{\theta}}{dt} = 0, \quad \frac{d\bar{\phi}}{dt} = \Omega(\bar{r}, \bar{\theta}) \tag{30}$$

where u_0 is set so that each spot takes 25 days to travel from $0.7R_\odot$ to the photosphere and $\Omega(\bar{r}, \bar{\theta})$ is the differential rotation as defined above. When the center of the spot reaches the photosphere, the spot is removed.

To apply the changes to the components of velocity, we first need to define the size of the emerging spot. As in [9], we define the radius of the spot as

$$\delta(\bar{r}) = \delta_0 \sqrt{\frac{R_\odot/\bar{r}_0 - 0.95}{R_\odot/\bar{r} - 0.95}} \tag{31}$$

where δ_0 is the initial radius of the perturbation caused by the spot when it is at $\bar{r} = \bar{r}_0 = 0.7R_\odot$, set as $\delta_0 = (5\pi/180)(0.7R_\odot)$ for all our simulations. The outward radial component of the velocity perturbation can then be defined as

$$\mathbf{U}_\tau = u_0 \exp\left(-\frac{\xi^2}{\delta^2}\right)\hat{\mathbf{e}}_r \tag{32}$$

and the vortical component of the velocity perturbation can be defined as

$$\mathbf{U}_\omega = -\frac{\omega_1 r}{2}\exp\left(-\frac{\xi^2}{\delta^2}\right)\sin\bar{\theta}\sin(\phi - \bar{\phi})\hat{\mathbf{e}}_\theta + \frac{\omega_1 r}{2}\exp\left(-\frac{\xi^2}{\delta^2}\right)(\sin\theta\cos\bar{\theta} - \cos\theta\sin\bar{\theta}\cos(\phi - \bar{\phi}))\hat{\mathbf{e}}_\phi \tag{33}$$

where $\omega_1 = -\omega_0 \cos\bar{\theta}$ and ω_0 is calibrated to tilt the spots according to the latitude they emerge at, which is found to be $\omega_0 = 0.08 \times 10^{-5} s^{-1}$ in [9]. There is also a diverging component of the flow included in the velocity perturbation, given as

$$\mathbf{U}_\rho = u_{\rho 0}\left(\frac{\xi}{R_\odot}\right)\frac{1}{2}\left(1 - \operatorname{erf}\left(\frac{\xi - \delta}{0.2\delta}\right)\right)\hat{\mathbf{e}}_\xi, \quad u_{\rho 0} = \frac{u_0}{2(\bar{r}/R_\odot)^2(R_\odot/\bar{r} - 0.95)}, \tag{34}$$

where $\hat{\mathbf{e}}_\xi$ is a radial unit vector centered at $(\bar{r}, \bar{\theta}, \bar{\phi})$ and $u_{\rho 0}$ is chosen to match the tube expansion rate in [9].

The final component we need to add to SD^2 is the definition of the boundary conditions at the photosphere and the base of the convective zone. Commonly, the lower boundary of the convective zone is assumed to be perfectly conducting, and the top boundary (the photosphere) is assumed to be either perfectly radial or matched to a potential field outside of the boundary. In this work, the bottom boundary is assumed to be perfectly conducting and the top boundary is taken to be perfectly radial. The perfectly conducting boundary is specified as

$$B_r = 0, \quad \frac{\partial(rB_\theta)}{\partial r} = 0, \quad \frac{\partial(rB_\phi)}{\partial r} = 0. \tag{35}$$

The perfectly radial boundary condition is specified as

$$B_\theta = 0, \quad B_\phi = 0, \tag{36}$$

which implies that $\frac{\partial(r^2 B_r)}{\partial r} = 0$ to maintain the $\nabla \cdot \mathbf{B} = 0$ condition.

For initialization, we slightly modify the initial conditions specified in section 5 of [9] to match our domain as

$$\mathbf{B} = \frac{B_0}{2}\left(\operatorname{erf}\left(\frac{r - 0.7R_\odot}{0.004R_\odot}\right) - \operatorname{erf}\left(\frac{r - 0.74R_\odot}{0.004R_\odot}\right)\right)\hat{\mathbf{e}}_\phi + \nabla \times (A_\phi \hat{\mathbf{e}}_\phi), \quad A_\phi = B_d \frac{\sin\theta}{r^3}\left(\frac{r - 0.7R_\odot}{R_\odot - 0.7R_\odot}\right) \tag{37}$$

where $B_0 = 250\text{G}$, $B_d = -0.008B_0$, and A_ϕ is set to 0 when $r < 0.7R_\odot$. We generate velocity perturbations according to the positions listed in the "Solar Region Summary" data archived by the NOAA National Centers for Environmental Information (NCEI) (`https://www.ngdc.noaa.gov/stp/space-weather/swpc-products/daily_reports/solar_region_summaries/`). We use the positions for bipolar regions with maximum solar area larger than 300 millionths of the solar photosphere. In an attempt to generate results similar to those in section 5 of [9], we take spots from August of 1996 to December of 2008. We set the $w_{spd} = 2$ and $\alpha = 0.01$.

B. Solar Dynamo Results

We validate SD^2 by running a simulation of Solar Cycle 23, from August 1996 to December 2008. The results we present first are the isosurfaces and Mollweide plots shown in Fig. 4. The panels at the top of Fig. 4 show the magnetic field at 1 year into the simulation, when there is little emergence activity. The panels on the bottom of Fig. 4 show the magnetic field at 5.4 years, which is around the maximum activity. We can see in Fig. 4a that the initial conditions are

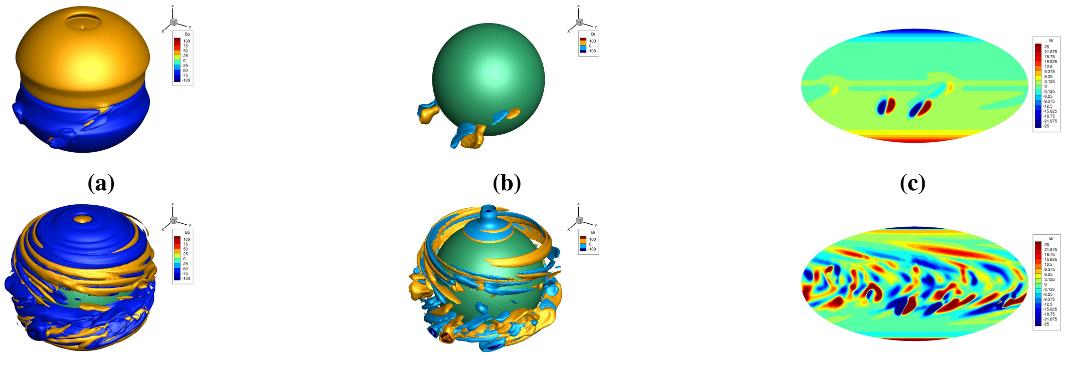

(a) **(b)** **(c)**

(d) **(e)** **(f)**

Fig. 4 Visualizations of B near the cycle minimum (1 year, panels a-c) and near cycle maximum (5.4 years, panels d-f). Panels (a) and (d) show B_ϕ between -125 and 125 G. Panels (b) and (e) show $\sqrt{B_r^2 + B_\theta^2}$, also between -125 and 125 G, where the sign of B_r is indicated by the color (red is positive, blue is negative). Panels (c) and (f) show B_r at the photosphere on a Mollweide equal-area projection, saturated at 25 G.

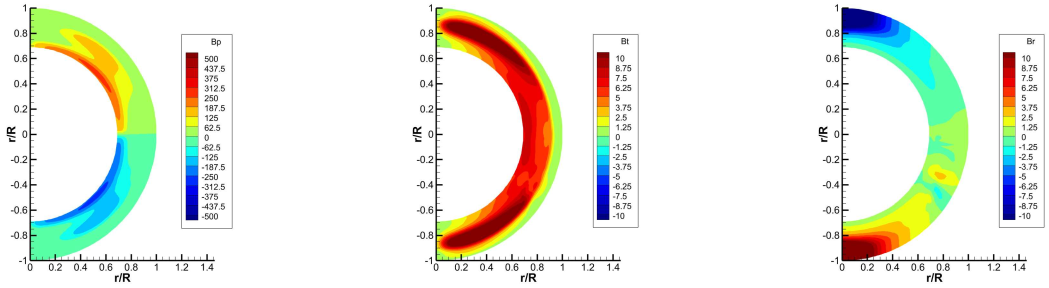

(a) B_ϕ **(b)** B_θ **(c)** B_r

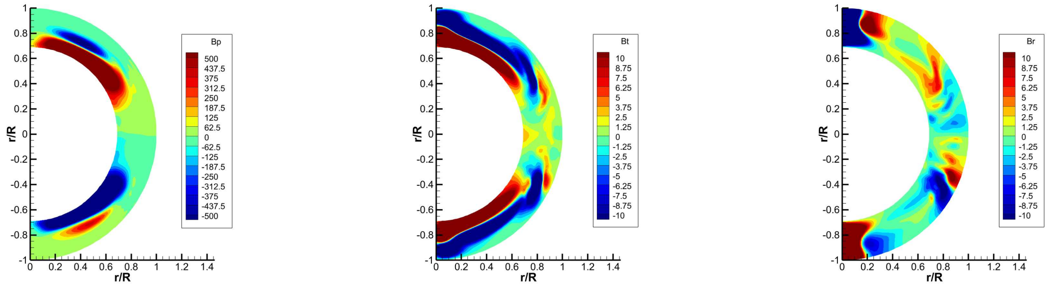

(d) B_ϕ **(e)** B_θ **(f)** B_r

Fig. 5 Longitude-averaged components of B at 1 year (panels a-c) and 5.4 years (panels d-f). All color axes are in Gauss.

still largely present, with disruptions where spots have emerged. Those spots can be seen in Fig. 4b as the poloidal components of the magnetic field, and their radial components are shown in Fig. 4c, which is a Mollweide projection at the photosphere. At maximum activity, the toroidal field in 4d shows multiple belts created by the many spots that have emerged, whose effects on the poloidal magnetic field can be seen in 4e and on the radial field at the photosphere in 4f.

Next, we assess the longitudinally averaged magnetic fields in Fig. 5, which better represent what is happening in the full domain. Again, the top row of panels shows results at 1 year and the bottom row shows results at 5.4 years of simulation. We can see the new toroidal field forming from Fig. 5a to Fig. 5d as an opposite-polarity field squishing the initial field against the lower boundary. The polar (B_θ) and radial (B_r) components of magnetic field also show the generation of new polarities of their fields, but the magnitude of the fields at the poles looks to be much higher

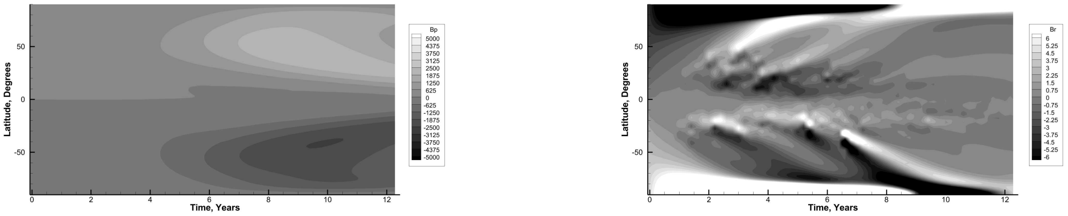

(a) $B_\phi(r = 0.7R_\odot)$ **(b)** $B_r(r = R_\odot)$

Fig. 6 Panel (a) shows longitude-averaged B_ϕ at $r = 0.7R_\odot$, while panel (b) shows longitude-averaged B_r at $r = R_\odot$ in Gauss.

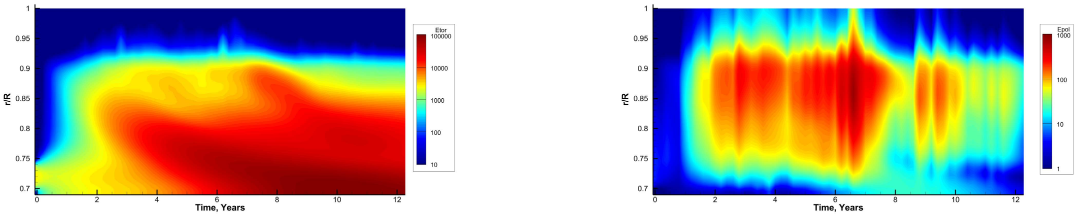

(a) E_{tor} **(b)** E_{pol}

Fig. 7 Panels (a) and (b) show the radial distributions of toroidal and poloidal magnetic energy density ($B_\phi^2/(8\pi)$ and $(B_r^2 + B_\theta^2)/(8\pi)$ respectively), averaged over θ and ϕ, as a function of time. A logarithmic color scale is used and units are ergs cm^{-3}.

than expected. We expect to see the polarity of the field in Fig. 5b stay at the poles for longer, but in Fig. 5e we see that the opposite polarity has already pushed the initial field away from the photosphere, and the transition between polarities does not look as smooth as we expect. In Fig. 5c the polarities of the radial field at the poles show the initial condition, but at the maximum activity shown in Fig. 5f the polarity at the poles is supposed to have almost finished flipping. Whitbread et al. [21] reports that adding a decay term to the induction equation makes a very small difference in the total unsigned surface flux but acts as a sink for the polar flux. Future tests should be conducted to see whether including this decay term will make the simulation SD^2 more realistic.

Butterfly diagrams are another common way to compare simulations with observations of solar activity, so we include butterfly diagrams in Fig. 6. Figure 6a shows the butterfly diagram of the toroidal magnetic field at $0.7R_\odot$, very close to our bottom boundary and the base of the convection zone. This figure is included to show that the toroidal field at the base of the convection zone starts to change at around the time of maximum activity and then tapers off as the solar cycle ends. Figure 6b shows the radial component of the magnetic field at the photosphere, from which it is obvious that the polarity of the radial magnetic field changes much later than observed (the polarity of the poles of the Sun was observed to change at about 5 years, while we simulated it changing at about 9 years), as we had suspected from Fig. 5f.

We also show radial averages of the toroidal (E_{tor}) and poloidal (E_{pol}) components of magnetic energy in Fig. 7, which are calculated as

$$E_{tor} = \frac{B_\phi^2}{8\pi}, \quad E_{pol} = \frac{B_r^2 + B_\theta^2}{8\pi}. \tag{38}$$

Figure 7a shows that the simulation starts with very little toroidal energy - mostly at the bottom of the convective zone - then additional toroidal energy is observed at larger radii. We expect to see two distinct belts in Fig. 7a, which would be belts of toroidal magnetic field of opposite signs as seen in Fig. 5d. Some reasons we cannot see these two belts could be that the radial resolution in the simulation is not fine enough to show the transition from one belt to the next, and/or because the bottom boundary does not allow the lower belt to fall below the tachocline, therefore making the distance between the belts too small to be seen in Fig. 7a. Comparing Fig. 7a with Fig. 7b, we can see that the toroidal energy starts to increase at about the same time that poloidal energy starts to get generated, as we expect from the Babcock Leighton (BL) mechanism. We can also see in Fig. 7b that poloidal energy is generated in the middle of the convective

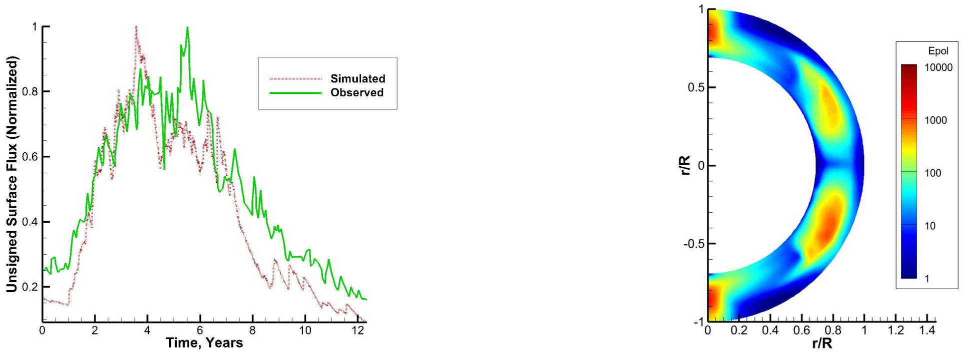

(a)

(b)

Fig. 8 Panel (a) shows surface fluxes (normalized to the maximum value) against time for the simulation and from observations. Panel (b) shows a longitude and time average of the poloidal magnetic energy density (in ergs cm^{-3}, logarithmic scale).

zone. These are good signs that the SD^2 simulation is working, as these results have been seen before in Yeates and Muñoz [9].

Finally, we have data on the unsigned surface flux and the time-averaged longitude-averaged poloidal energy, both shown in Fig. 8. We can see in Fig. 8a that the shape of the time history of the unsigned surface flux mostly matches what has been observed, although the peak is simulated to be 2 years before it was observed. This is likely because we are only taking spots of a certain size that are bipolar, so the effects of smaller spots are neglected in the simulation, although we would like to simulate the peak unsigned flux at the same time as it was observed. In Fig. 8b, we can see that the poloidal energy is generated at the latitudes where the spots emerge, which shows that the emergence of the spots is responsible for the generation of poloidal energy, as we suspected from Fig. 7b.

V. Conclusions

The spectral difference method with divergence cleaning can be used to simulate kinematic solar-dynamo problems, though there are some issues that should be resolved before it can be relied on. Generally, the structures and magnitudes produced by the spectral difference solar dynamo (SD^2) code are reasonable, so we believe that in time SD^2 can be tuned to produce solar cycles closer to those that have been simulated and observed. The biggest issue with the SD^2 code at the moment is that the poles have a lot more activity than other simulations suggest (such as the one in Section 5 of Yeates and Munoz [9]), and that the poles do not change polarity when we expect them to.

VI. Future Work

The next step for the SD^2 code is the addition of a magnetic decay term as proposed by Whitbread et al. [21], which is reported to mostly dampen activity at the poles. Other work that should be done is the creation of a mesh that can resolve the magnetic diffusivity profile, which will hopefully allow for more realistic simulations and use of higher order methods. We intend to apply the experience gained from designing the SD^2 code to full MHD simulations of the solar dynamo, although kinematic dynamo simulations will always be more efficient and therefore more practical for real-world use.

Acknowledgments

Both authors would like to acknowledge the financial support of a National Science Foundation (NSF) award (No. 2310372) monitored by Dr. Lisa Winter and an Air Force Office of Scientific Research (AFOSR) grant (award No. FA9550-23-1-0596) monitored by Dr. Fariba Fahroo. The authors thank Dr. Mark Miesch of the National Oceanic and Atmospheric Administration (NOAA) for many fruitful discussions of this research. Resources supporting this work were provided by the NASA High-End Computing (HEC) Program through the NASA Advanced Supercomputing (NAS) Division at Ames Research Center.

References

[1] Kopriva, D. A., "Multidomain Spectral Solution of Compressible Viscous Flows," *Journal of Computational Physics*, Vol. 115, No. 1, 1994, pp. 184–199.

[2] Sun, Y., Wang, Z. J., and Liu, Y., "High-Order Multidomain Spectral Difference Method for the Navier-Stokes Equations on Unstructured Hexahedral Grids," *Communications in Computational Physics*, Vol. 2, 2007, pp. 310–333.

[3] Liang, C., Jameson, A., and Wang, Z. J., "Spectral difference method for compressible flow on unstructured grids with mixed elements," *Journal of Computational Physics*, Vol. 228, 2009, pp. 2847–2858.

[4] Chen, K., and Liang, C., "An Arbitrarily High-order Spectral Difference Method with Divergence Cleaning (SDDC) for Compressible Magnetohydrodynamic Simulations on Unstructured Grids," *The Astrophysical Journal*, Vol. 932, No. 1, 2022, p. 16.

[5] Hankey, R., Chen, K., and Liang, C., "Extending the Spectral Difference Method with Divergence Cleaning (SDDC) to the Hall MHD Equations," *Northeast Journal of Complex Systems (NEJCS)*, Vol. 5, No. 1, 2023.

[6] Biswas, S., and Ganesh, R., "Effect of flow shear on the onset of dynamos," *Physics of Plasmas*, Vol. 30, No. 11, 2023, p. 112902.

[7] Chen, K., Liang, C., and Wan, M., "Arbitrarily high-order accurate simulations of compressible rotationally constrained convection using a transfinite mapping on cubed-sphere grids," *Physics of Fluids*, Vol. 35, No. 8, 2023, p. 086120.

[8] Miesch, M. S., and Teweldebirhan, K., "A three-dimensional Babcock–Leighton solar dynamo model: Initial results with axisymmetric flows," *Advances in Space Research*, Vol. 58, No. 8, 2016, pp. 1571–1588. Solar Dynamo Frontiers.

[9] Yeates, A. R., and Muñoz-Jaramillo, A., "Kinematic active region formation in a three-dimensional solar dynamo model," *Monthly Notices of the Royal Astronomical Society*, Vol. 436, No. 4, 2013, pp. 3366–3379.

[10] Miesch, M. S., and Dikpati, M., "A Three-Dimensional Babcock–Leighton Solar Dynamo Model," *The Astrophysical Journal Letters*, Vol. 785, No. 1, 2014, p. L8.

[11] Karak, B. B., and Miesch, M. S., "Solar Cycle Variability Induced by Tilt Angle Scatter in a Babcock–Leighton Solar Dynamo Model," *The Astrophysical Journal*, Vol. 847, No. 1, 2017, p. 69.

[12] Derigs, D., Winters, A. R., Gassner, G. J., Walch, S., and Bohm, M., "Ideal GLM-MHD: About the entropy consistent nine-wave magnetic field divergence diminishing ideal magnetohydrodynamics equations," *Journal of Computational Physics*, Vol. 364, 2018, pp. 420–467.

[13] Powell, K. G., Roe, P. L., Linde, T. J., Gombosi, T. I., and De Zeeuw, D. L., "A Solution-Adaptive Upwind Scheme for Ideal Magnetohydrodynamics," *Journal of Computational Physics*, Vol. 154, No. 2, 1999, pp. 284–309.

[14] Rusanov, V., "The calculation of the interaction of non-stationary shock waves and obstacles," *USSR Computational Mathematics and Mathematical Physics*, Vol. 1, No. 2, 1962, pp. 304–320.

[15] Lax, P. D., "Weak solutions of nonlinear hyperbolic equations and their numerical computation," *Communications on Pure and Applied Mathematics*, Vol. 7, No. 1, 1954, pp. 159–193.

[16] Bassi, F., and Rebay, S., "A High-Order Accurate Discontinuous Finite Element Method for the Numerical Solution of the Compressible Navier–Stokes Equations," *Journal of Computational Physics*, Vol. 131, No. 2, 1997, pp. 267–279.

[17] Ruuth, S. J., "Global Optimization of Explicit Strong-Stability-Preserving Runge-Kutta Methods," *Mathematics of Computation*, Vol. 75, No. 253, 2006, pp. 183–207.

[18] Dikpati, M., Gilman, P. A., de Toma, G., and Ulrich, R. K., "Impact of changes in the Sun's conveyor-belt on recent solar cycles," *Geophysical Research Letters*, Vol. 37, No. 14, 2010.

[19] Dikpati, M., "POLAR FIELD PUZZLE: SOLUTIONS FROM FLUX-TRANSPORT DYNAMO AND SURFACE-TRANSPORT MODELS," *The Astrophysical Journal*, Vol. 733, No. 2, 2011, p. 90.

[20] Karak, B., and Cameron, R., "BABCOCK–LEIGHTON SOLAR DYNAMO: THE ROLE OF DOWNWARD PUMPING AND THE EQUATORWARD PROPAGATION OF ACTIVITY," *The Astrophysical Journal*, Vol. 832, No. 1, 2016, p. 94.

[21] Whitbread, T., Yeates, A. R., and Muñoz-Jaramillo, A., "The need for active region disconnection in 3D kinematic dynamo simulations," *A&A*, Vol. 627, 2019, p. A168.